

Electrochemical and Mechanistic Study of Oxidative Degradation of Favipiravir by Electrogenerated Superoxide through Proton-Coupled Electron Transfer

Tatsushi Nakayama* and Ryo Honda

Cite This: <https://doi.org/10.1021/acsomega.1c03230>

Read Online

ACCESS |



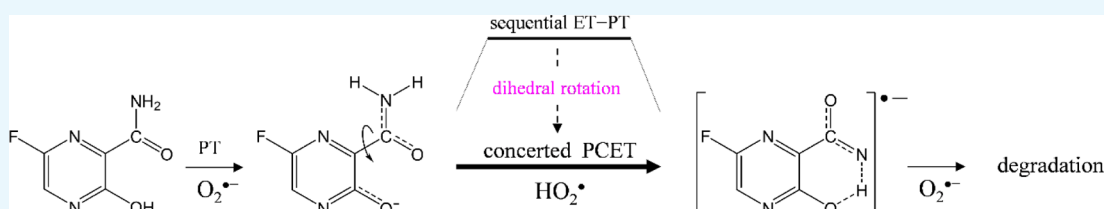
Metrics & More



Article Recommendations



Supporting Information



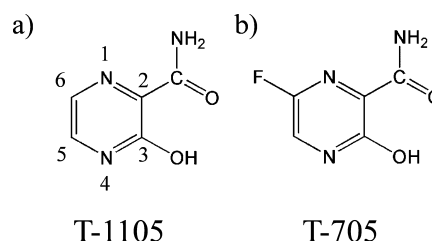
ABSTRACT: Electrochemical analyses aided by density functional theory calculations were used to investigate the oxidative degradation of pyrazine antiviral drugs, 3-hydroxypyrazine-2-carboxamide (T-1105) and 6-fluoro-3-hydroxypyrazine-2-carboxamide (favipiravir, T-705), by the electrogenerated superoxide radical anion ($\text{O}_2^{\bullet-}$). T-1105 and T-705 are antiviral RNA nucleobase analogues that selectively inhibit the RNA-dependent RNA polymerase. They are expected as a drug candidate against various viral infections, including COVID-19. The pyrazine moiety was decomposed by $\text{O}_2^{\bullet-}$ through proton-coupled electron transfer (PCET). Our results show that its active form, pyrazine-ribofuranosyl-5'-triphosphate, is easily oxidized under inflamed organs by overproduced $\text{O}_2^{\bullet-}$ through the PCET mechanism in the immune system. This mechanistic study implies that the oxidative degradation of pyrazine derivatives will be prevented by controlling the PCET through simple modification of the pyrazine structure.

1. INTRODUCTION

The development of therapeutic medicines against the newly pathogenic severe acute respiratory syndrome coronavirus 2 (SARS-CoV-2) is desired considering the current COVID-19 pandemic.¹ However, developing a highly efficient antiviral drug against a new virus in which virus-type mutations occur frequently or whose characteristics are unknown properties is difficult. Therefore, the development of new antiviral drugs with a broad spectrum and certain effectiveness for various viral mutations is required. To identify a promising candidate drug to treat COVID-19, structural modification of the existing several RNA nucleobase analogues is an effective development method, such as remdesivir,^{2,3} ribavirin,⁴ brincidofovir,⁵ and favipiravir; 6-fluoro-3-hydroxypyrazine-2-carboxamide (favipiravir, T-705) is sold under the brand name avigan⁶ (Chart 1).

Pyrazine derivatives such as T-705,^{7–9} 3-hydroxypyrazine-2-carboxamide (T-1105),^{10,11} and 3,4-dihydro-3-oxo-4- β -D-ribofuranosyl-2-pyrazinecarboxamide (T-1106)¹² block the replication of many RNA viruses, including arenaviruses (Junin, Machupo, and Pichinde), and are expected to be an effective antiviral drug for COVID-19. The selective inhibition of viral RNA-dependent RNA polymerase (RdRp) is assumed to be the mechanism of action for their anti-SARS-CoV-2.^{13,14} Their antiviral effects are based on the fact that the viral RNA polymerase mistakenly recognizes the 3-hydroxypyrazine-2-carboxamide-ribofuranosyl-5'-triphosphate (pyrazine-RTP) structure as a purine nucleotide (adenosine and guanosine).

Chart 1. Structures of the Antiviral Drugs Considered in This Study^a



^a(a) 3-Hydroxypyrazine-2-carboxamide (T-1105) and (b) 6-fluoro-3-hydroxypyrazine-2-carboxamide (favipiravir; T-705).

Thus, they prevent virus multiplication with purine analogue effects as RdRp inhibitors. Since RdRp domains are not present in human cells and are conserved among RNA viruses, this distinct specific mechanism targeting RNA viral

Received: June 21, 2021

Accepted: August 3, 2021

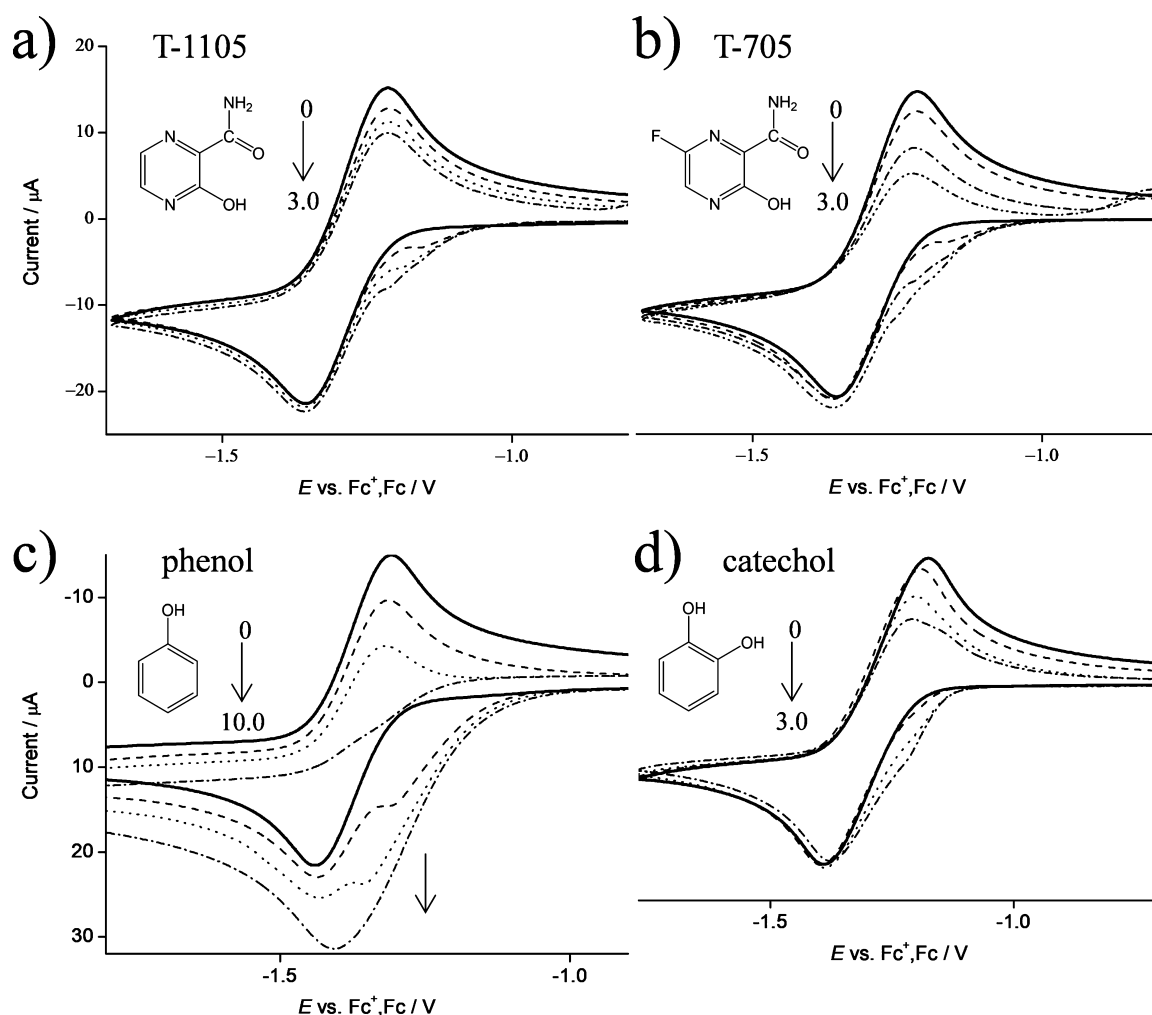


Figure 1. CVs of O_2 ($4.8 \times 10^{-3} \text{ mol dm}^{-3}$) in the presence of (a) T-1105, (b) T-705, (c) phenol, and (d) catechol, in DMF containing 0.1 mol dm^{-3} TPAP, recorded with a GC electrode ($\Phi = 1.0 \text{ mm}$) at a scan rate of 0.1 V s^{-1} . Concentrations ($\times 10^{-3} \text{ mol dm}^{-3}$) are 0, 1.0, 2.0, and 3.0 (a,b,d), and 0, 3.0, 5.0, and 10.0, (c) (the concentration changes are shown by arrows).

polymerases makes pyrazine derivatives an attractive drug candidate.

With its mechanism of action and a broad range of antiviral activity, the pyrazine-structural drugs (T-1105 or its more active derivative: T-705) are promising drug candidates for RNA viral diseases, including COVID-19. T-705 is now expected to conduct clinical trials for use against COVID-19 worldwide, although there is a fatal issue that the antiviral effect is weak *in vivo*, where a high dose is needed for potential antiviral activity.¹⁵ T-1105 is a prodrug, which needs to be metabolized to its active form, pyrazine-RTP.¹¹ Then, pyrazine-RTP prevents virus multiplication by their analogue effect but cannot kill the virus.^{11,16} Therefore, the immune response must be used to kill the virus while also preventing it from multiplying.¹⁷ Considering these biological conditions for its mechanism of action *in vivo*, the effective concentration of its active form after the metabolization will be lower, although T-705 is available in both oral and intravenous formulations.^{7,9,11} Regarding the favipiravir as a prodrug of the RNA polymerase inhibitor, the purpose is to supply favipiravir-RTP; the active form is a purine nucleic acid analogue vicinity of the virus in inflamed organs such as the lung. However, if most of the dosed T-705 is decomposed during the conversion processes to the active form and drug delivery, the

concentration near the virus drops to a level where the desired antiviral effect cannot be obtained. Therefore, if the concentration of T-705-RTP can be increased by inhibiting T-705 metabolic degradation, the antiviral efficacy can be enhanced.⁹

COVID-19 has characteristic symptoms caused by SARS-CoV-2. While most cases result in mild symptoms, some progress to viral pneumonia and multiorgan failure.^{2,4,18,19} To prevent this serious symptom, it is necessary to prevent the proliferation of SARS-CoV-2 and suppress the immune reaction that causes inflammation. As a drug therapy, it is highly possible that an RNA replication inhibitor such as T-705 alone cannot have an immediate effect because it can stop the multiplication of SARS-CoV-2 but cannot eliminate the existing virus. Therefore, an RNA replication inhibitor requires a combination of immunity, thus, with an unavoidable immune inflammation.

A system involving numerous proteins and cells such as neutrophils, macrophages, killer T cells, and various cytokines has been established in the immune system of the living body to contribute to infection defense.^{20–23} Neutrophils and macrophages, the center of the immune system, phagocytose foreign pathogenic viruses that have infiltrated the body and use reactive oxygen species (ROS) to oxidize and decompose

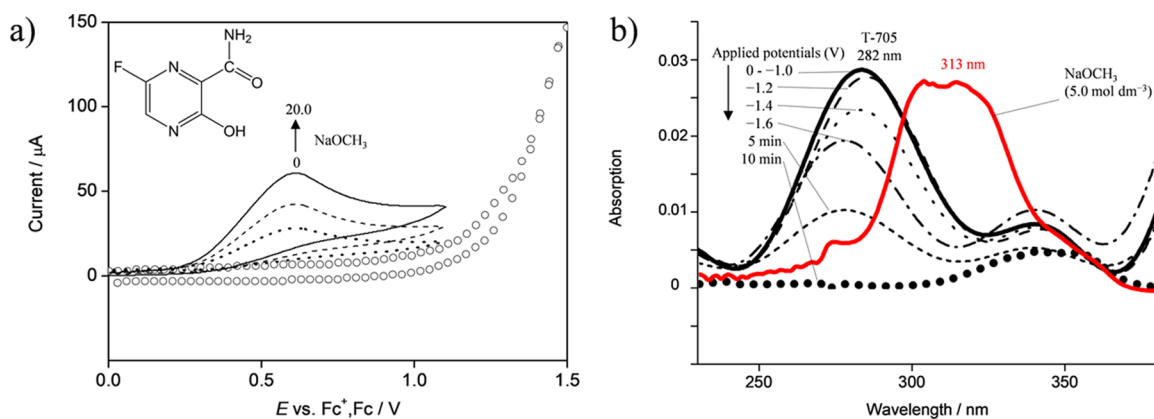


Figure 2. (a) CVs of T-705 ($10.0 \times 10^{-3} \text{ mol dm}^{-3}$) in the absence (circle) and in the presence of CH_3ONa (0, 5.0, 10.0, and $20.0 \times 10^{-3} \text{ mol dm}^{-3}$) in DMF containing 0.1 mol dm^{-3} TPAP recorded with a GC electrode ($\Phi = 1.0 \text{ mm}$) at a scan rate of 0.1 V/s . (b) UV-vis spectral changes in T-705 ($1.0 \times 10^{-3} \text{ mol dm}^{-3}$) solutions in the absence (black bold) and presence (red bold) of CH_3ONa ($5.0 \times 10^{-3} \text{ mol dm}^{-3}$) and *in situ* electrolytic UV-vis spectra of T-705 in the presence of saturated O_2 . The controlled potential at -1.0 , -1.2 , -1.4 , and $-1.6 \text{ V vs Fc}^+/\text{Fc}$ was applied to the solutions.

them. Thus, the superoxide radical anion ($\text{O}_2^{\bullet-}$), the center of the ROS family in the terminal of the immune mechanism, is produced and oxidatively decomposes foreign substances such as viruses.²² However, it is said that when excessively produced $\text{O}_2^{\bullet-}$ attacks cells, it induces tissue inflammation. Therefore, immune oxidation must be used to break out the virus while also keeping it from multiplying, and an analogue drug that acts under inflammatory conditions is required. In an inflamed organ, the degradation and inactivation of analogue drugs due to the ROS redox reaction under the immune system are inevitable. Therefore, it is important to know the redox reaction between ROS and antiviral drugs in preventing its degradation and maximizing the concentration at the inflamed organ.

Several redox mechanisms between $\text{O}_2^{\bullet-}$ and acidic substrates such as T-705 are known, such as superoxide-facilitated oxidation (SFO),^{24–26} hydrogen-atom transfer involving proton-coupled electron transfer (PCET),^{27–31} and sequential proton-loss ET.³² In the SFO mechanism, the initial proton transfer (PT) from the substrate to $\text{O}_2^{\bullet-}$ to give a hydroperoxyl radical (HO_2^{\bullet}) is followed by rapid dismutation to give hydroperoxide (H_2O_2) and dioxygen (O_2). Then, the substrate anion is oxidized by the O_2 formed in the dismutation process.³³ Conversely, the other two mechanisms involve direct oxidation by $\text{O}_2^{\bullet-}$ or HO_2^{\bullet} . Considering the possible mechanisms and structure-decomposability relationship of T-705, its T-1105 moiety is thought to play a significant role in the oxidative decomposition mechanism. Our previous studies reported that $\text{O}_2^{\bullet-}$ is eliminated by polyphenols,³⁰ 1,4- and 1,2-benzendiols (hydroquinone²⁹ and catechol²⁸), and monophenols including aminophenols^{31,34} through the oxidative ET involved in the PCET. In these studies, the PCET mechanism is based on quinone-hydroquinone π -conjugation and involves two PTs and one ET.

In the present study, we have conducted a mechanistic analysis based on electrochemistry and theoretical calculations on the reactivity between T-705 (T-1105) and electro-generated $\text{O}_2^{\bullet-}$. Accordingly, we present valuable information regarding the degradation of pyrazine antiviral RNA-analogue drugs by $\text{O}_2^{\bullet-}$, which is assumed to be important to manage the concentrations of antiviral drugs in an inflamed organ. It is hoped that this study provides an insight into the antiviral drugs that are not easily metabolized, thereby expanding the

point to consider drug design and utility, such as enhancement of net pharmacological activity and reduction of side effects associated with less dosage.

2. RESULTS AND DISCUSSION

2.1. Reactivity between Electrogenerated $\text{O}_2^{\bullet-}$ and Pyrazine Antiviral Drugs.

2.1.1. CV of $\text{O}_2/\text{O}_2^{\bullet-}$ in the Presence of Pyrazine Antiviral Drug.

Based on electrochemical measurements in *N,N*-dimethylformamide (DMF), the reactivity between pyrazine antiviral drugs and $\text{O}_2^{\bullet-}$ was discussed (Supporting Information, Figure S1). Figure 1 shows the cyclic voltammograms (CVs) for saturated O_2 ($4.8 \times 10^{-3} \text{ mol dm}^{-3}$) in the presence of T-1105 (a), T-705 (b), phenol (c), and catechol (d). The CVs obtained in the presence of phenol and catechol were reported in our previous paper^{28–31} and are presented here for comparison to show the CV behavior, demonstrating an ET between $\text{O}_2^{\bullet-}$ and the substrate. In aprotic and unbuffered solvents such as DMF, O_2 shows quasi-reversible redox at -1.284 V versus the ferrocenium ion/ferrocene (Fc^+/Fc) couple (eq 1), resulting in the formation of $\text{O}_2^{\bullet-}$ in the initial cathodic scan and reoxidation to O_2 in the returned anodic scan (solid lines, Figure 1a–d). The reversible CVs investigated here were all modified to irreversible CVs with a loss of anodic current by the presence of the protic compounds (a–d) in a concentration-dependent manner, suggesting that the initial homogeneous reaction between electrogenerated $\text{O}_2^{\bullet-}$ and the compounds is PT. This result is supported by the fact that the CV traces in the absence of O_2 [removed by bubbled dinitrogen (N_2)] show no peaks over the potential range investigated (data not shown). Thus, the loss of reversibility in the $\text{O}_2/\text{O}_2^{\bullet-}$ is due to the PT from the compounds forming HO_2^{\bullet} (eq 2).

In the presence of phenol (Figure 1c), the bioelectronic CV with an additional prepeak on the cathodic scan was observed, which is driven by the exergonic reduction of the resulting HO_2^{\bullet} /hydroperoxyl anion (HO_2^-) after the primary electrode process associated with PT, leading to the irreversible overall reduction of O_2 to H_2O_2 . Conversely, in the presence of pyrazine antiviral drugs (a, b), the CV traces do not show bioelectronic characteristics owing to the elimination of HO_2^{\bullet} by those anions (T-1105⁻ and T-705⁻) through the

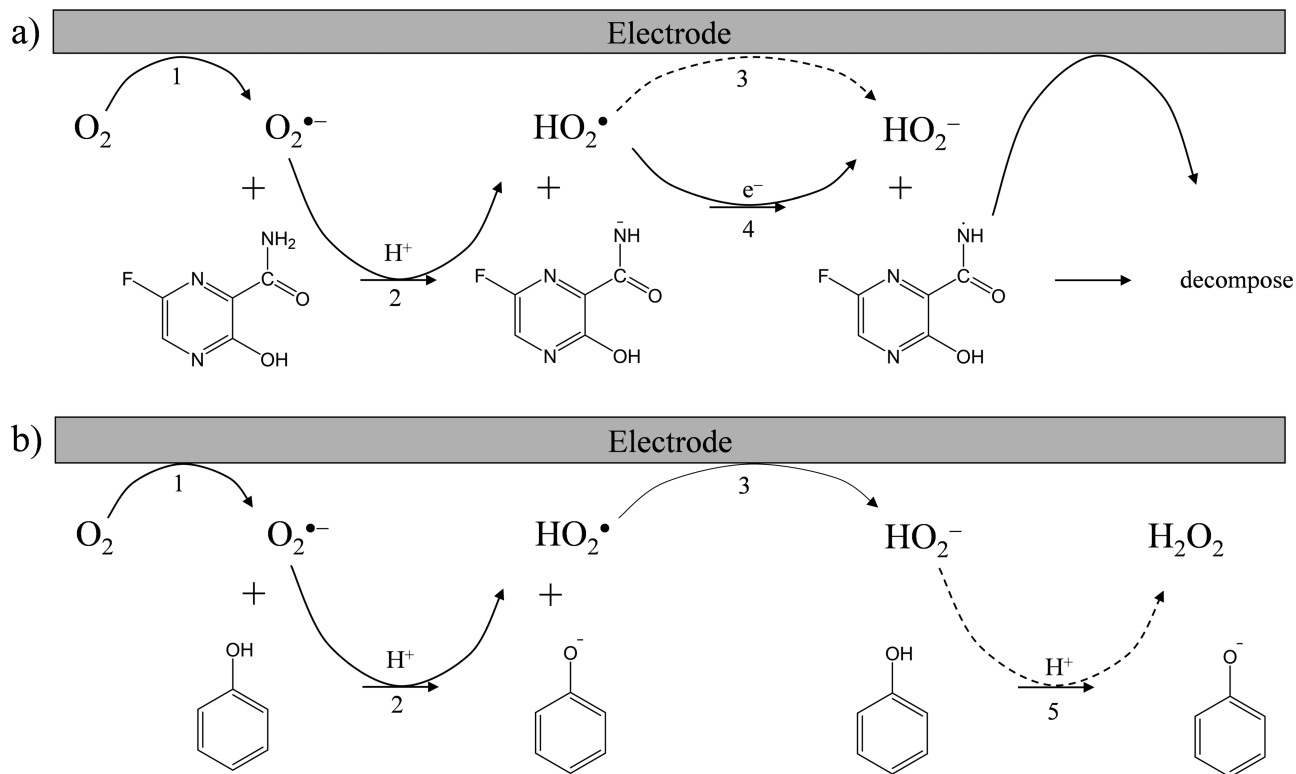
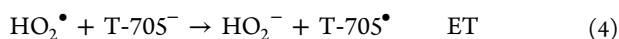
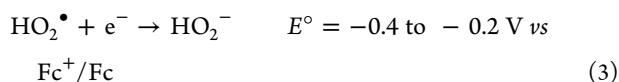
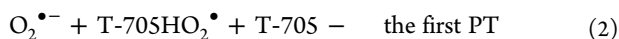
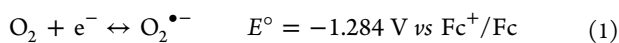


Figure 3. Plausible electrochemical mechanism for $\text{O}_2/\text{O}_2^{\bullet-}$ in the presence of (a) T-705 and (b) phenol in DMF. ¹One-electron reduction of $\text{O}_2/\text{O}_2^{\bullet-}$; ²the first PT from the acidic substrate to $\text{O}_2^{\bullet-}$; ³one-electron reduction of $\text{HO}_2^{\bullet}/\text{HO}_2^-$; ⁴ET from the substrate anion to HO_2^{\bullet} ; and ⁵the second PT to HO_2^- .

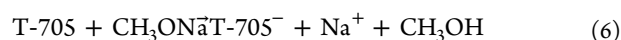
subsequent ET (eq 4) forming the corresponding radicals (T-1105[•] and T-705[•]), similar to that in the presence of catechol (d). As a CV result, Figure 1a,b demonstrates that T-1105 and T-705 were chemically oxidized by $\text{O}_2^{\bullet-}$, through the first PT and subsequent ET.



where E° (V vs Fc^+/Fc) is the standard redox potential.

2.1.2. In Situ Electrolytic UV-vis Spectral Analysis of Reactivity between Pyrazine Antiviral Drugs and $\text{O}_2^{\bullet-}$. The reactivity between T-705 and electrogenerated $\text{O}_2^{\bullet-}$ was confirmed, through *in situ* electrolytic ultraviolet-visible (UV-vis) spectral measurements using the optically transparent thin-layer electrochemical (OTTLE) cell (Supporting Information, Figure S2). First, the electrochemical oxidation of T-705 at a glassy carbon (GC) electrode in a DMF solution under purging N_2 was conducted using cyclic voltammetry (Figure 2a). Over the accessible potential range (+1.5 to 0 V vs Fc^+/Fc) in DMF, no peak was observed for the oxidation of T-705 but for the electrolysis of the DMF solvent ($E_{\text{pa}} = 1.2 \text{ V vs Fc}^+/\text{Fc}$, shown by a circle). Next, sodium methoxide (CH_3ONa) as a Brønsted base (an alkali agent) was added to the solution, and an anodic peak appeared at around 0.55 V

in the CVs with the concentration dependency (the voltammetric behavior was the same for T-1105). Therefore, the observed anodic peak will derive from the oxidation of T-705⁻ generated after deprotonation by CH_3ONa (eq 6). The observed CV was irreversible and broadened, implying that the deprotonated T-705⁻ was irreversibly oxidized at more than one electron and chemically irreversible to a starting material, that is, the deprotonated T-705⁻ is easily decomposed on the electrode surface through base-catalyzed oxidation. Although details of the electrochemical mechanism causing the broaden peak are unclear, the fact that some oxidation mechanisms related to the acid–base reaction, that is, sequential proton–ET (PT–ET) and concerted PT–ET, are possible remains controversial.



Considering these CV results, *in situ* electrolytic UV-vis spectra for the CV solution containing T-705 ($1.0 \times 10^{-3} \text{ mol dm}^{-3}$) were measured in the absence of O_2 under purging N_2 and in the presence of O_2 (b). The spectrum of T-705 alone has a characteristic absorption band centered at 282 nm. Under the applied potential at +1.5 to -2.0 V vs Fc^+/Fc without O_2 , the spectrum did not change where any potential was applied (data not shown), demonstrating that T-705 is not electrolyzed without deprotonation, which is in reasonable agreement with CV results shown in Figure 2a. Conversely, the spectrum has changed in the presence of CH_3ONa ($5.0 \times 10^{-3} \text{ mol dm}^{-3}$) without applying a potential (red line). Since T-705 is deprotonated by CH_3ONa as a Brønsted base, the spectrum centered at 313 nm will be attributed to T-705⁻, showing a spectrum shift.

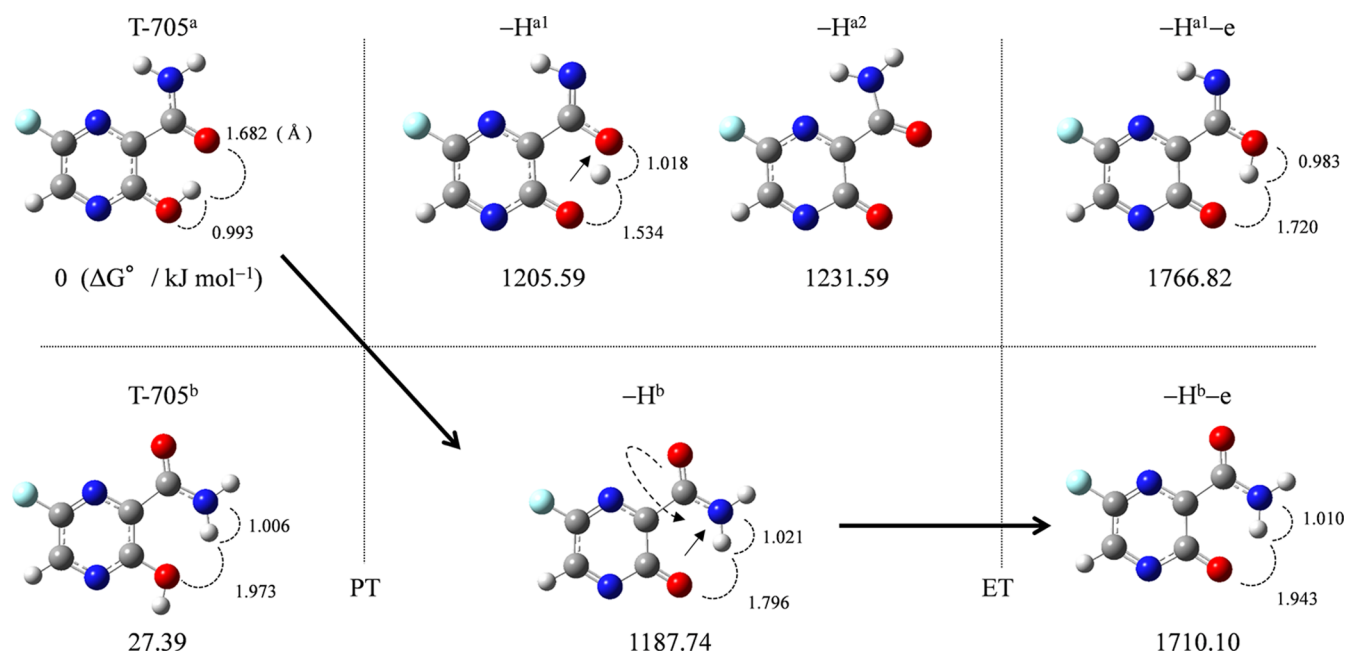


Figure 4. Different conformers of T-705 (T-705^a and T-705^b), T-705⁻ (-H¹, -H², and -H^b), and T-705[•] (-H¹-e and -H^b-e) along the PCET reaction—calculated DFT-(U)B3LYP/PCM/6-311+G(3df,2p) in DMF, denoted by calculated ΔG° s for each chemical species (kJ mol⁻¹, 298.15 K) and bond length of intramolecular HBs (Å).

On the other side, the spectrum of T-705 in the presence of saturated O₂ (4.8×10^{-3} mol dm⁻³) has changed, decreasing the intensity at applied cathodic potentials over -1.3 V corresponding electrogeneration of O₂^{•-} (Figure 2c). Furthermore, keeping the potential at -1.6 V for 10 min, the spectrum of T-705 disappeared. These spectral changes have demonstrated that the product of homogeneous reaction between T-705 and O₂^{•-} is not T-705⁻. By analogy with the CV results, the initial PT (eq 2) and the following reactions including ET between HO₂[•] and T-705⁻ (eq 4) rapidly undergo base-catalyzed oxidation, resulting in degradation of T-705/T-705⁻. Measured in the OTTLE cell having a 1.0 mm thin layer, the spectra immediately disappeared when the potential was applied. Thus, the following reactions will proceed in a superior kinetics via the intermediates, T-705⁻ and T-705[•], otherwise concertedly with the initial PT. Since the radical product was undetectable using the *in situ* electrolytic electron spin resonance (ESR) system (Supporting Information, Figure S2), T-705[•] would be decomposed at the subsequent reaction (no data are shown). These series of reactions, the initial PT (eq 2) followed by the subsequent oxidation and others, are referred to as the base-catalyzed oxidation process or the SFO.^{24,25} The SFO is the oxidation of the substrate anion (generated by alkali O₂^{•-}) by O₂. When considering the superior kinetic expected from the CV and *in situ* spectral results, the mechanism will involve the sequential ET from T-705⁻ to HO₂[•] coupled to the initial PT, that is, PCET, rather than SFO. As a result of the spectral measurements, the degradation of T-705 by O₂^{•-} through the PCET was shown.

As shown above, the CV traces for O₂/O₂^{•-} in the presence of the compounds are divided into two typical curves: type A, an irreversible one-electron process (eqs 1, 2, and 4) leading to O₂^{•-} elimination, which is typically observed with the catechol moiety as reported in our previous paper. Also, type B, an irreversible two-electron process observed in electro-chemical-electro reactions (eqs 1–3). In this scenario, Figure 3

shows the plausible electrochemical mechanisms for O₂/O₂^{•-} in the presence of (a) T-705 (type A) and (b) phenol (type B), summarizing eqs 1–5. Furthermore, type A involves efficient PT–ET between T-705 and O₂^{•-} through the PCET mechanism, resulting in degradation of T-705.

2.2. DFT Analyses of the PCET Reaction between Pyrazine Antiviral Drugs and O₂^{•-}. **2.2.1. Optimization of Stable Structures of T-705 and Its Corresponding Chemical Species along the PCET.** Density functional theory (DFT) calculations were performed with the Becke three-parameter Lee–Yang–Parr (B3LYP) hybrid functional employing the polarized continuum model (PCM) method to aid the mechanistic analysis of the PCET between pyrazine antiviral drugs (T-1105 and T-705) and O₂^{•-} in DMF. First, to obtain the structures of the stable conformer of T-705 and its corresponding chemical species along the PCET, energy scanning for the dihedral angle around the 2-carboxamide group was performed. Figure 4 shows the optimized structures of two T-705-conformers (T-705^a and T-705^b), the T-705⁻ upon initial PT (-H¹, -H², and -H^b) and the T-705[•] after the subsequent ET (-H¹-e and -H^b-e). Calculated standard Gibbs free energy changes (ΔG° /kJ mol⁻¹, 298.15 K) for the chemical species and bond length (Å) of intramolecular hydrogen bonds (HBs) are denoted.

T-705 has two planar conformers (T-705^a and T-705^b) that differ in the orientation of the dihedral angle around the 2-carboxamide group, forming an intramolecular HB between the adjacent 3-hydroxyl group. Comparison of the ΔG° s shows that T-705^a is more stable than T-705^b by 27.39 kJ mol⁻¹. Therefore, the 2-carboxamide proton of T-705^a will be deprotonated upon the initial PT because the 3-hydroxyl proton is forming HB. However, the stable conformers for both of the T-705⁻ and T-705[•] were T-705^b derivatives, -H^b (1187.74) and -H^b-e (1710.10), respectively. Thus, these calculation results imply that the 2-carboxamide group rotates along the initial PT process of the PCET. Furthermore, the 3-hydroxyl proton will be gravitated toward the 2-carboxamide

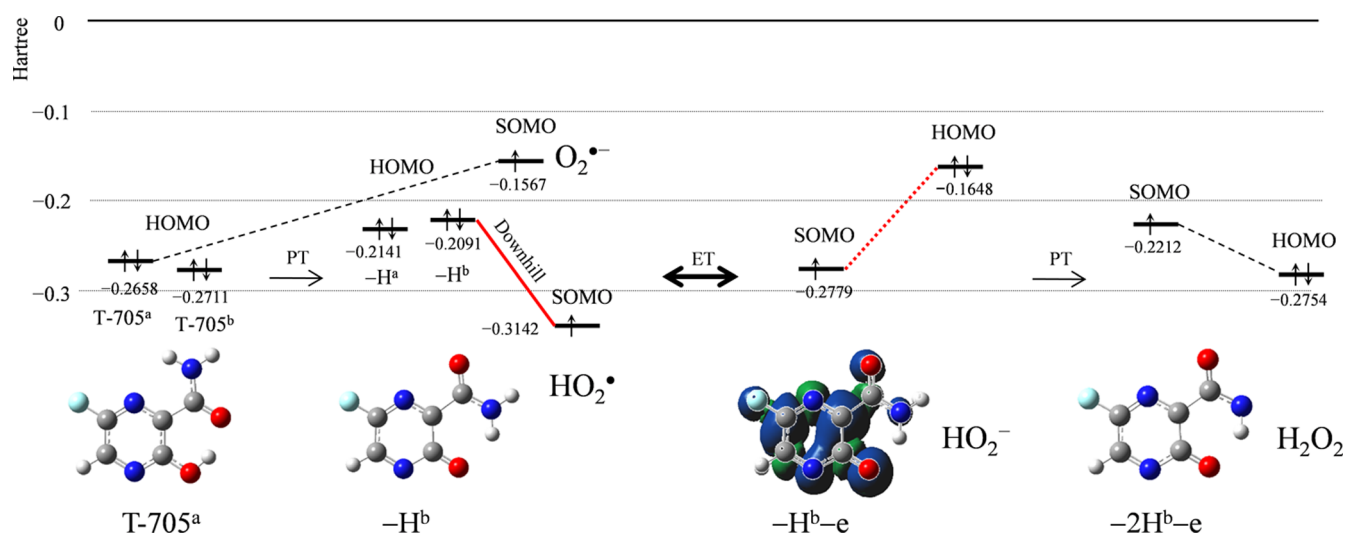


Figure 5. Change in HOMO–LUMO energies (Hartree) upon PCET between $O_2^{\bullet-}$ and two conformers of T-705 (T-705^a and T-705^b) with their corresponding chemical species in DMF, calculated with the DFT-(U)B3LYP/PCM/6-311+G(3df,2p).

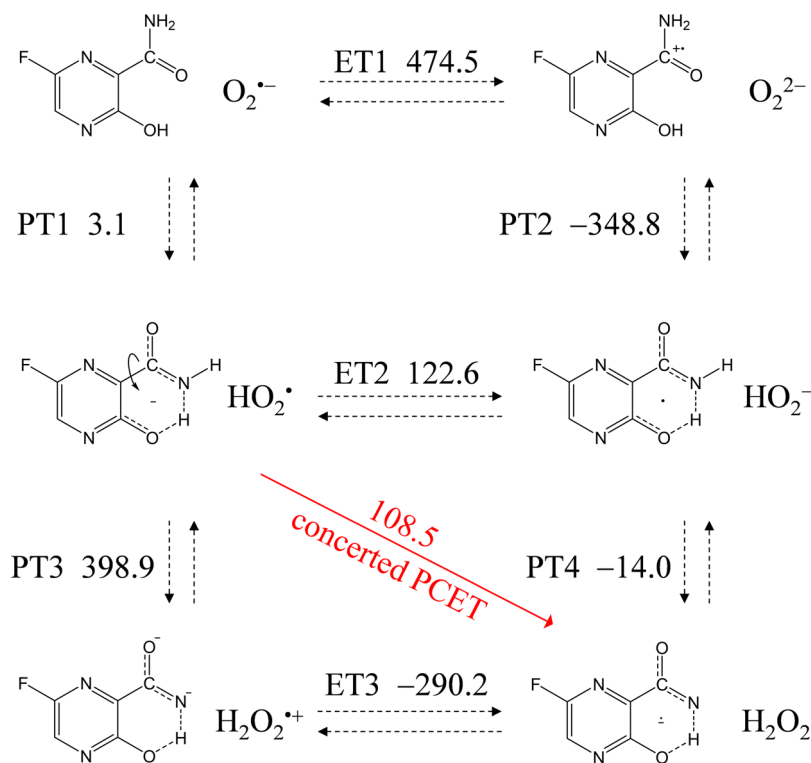


Figure 6. Six diabatic electronic states and the ΔG° values for the PCET between T-705 and $O_2^{\bullet-}$ involving two PTs and one ET in DMF. ΔG° (kJ mol⁻¹, 298.15 K) for PT (PT1–PT4), ET (ET1–ET3), and concerted PCET were calculated using the DFT-(U)B3LYP/PCM/6-311+G(3df,2p) method.

side after its rotation, forming $-H^b$ (bond lengths (Å), N–HO: 1.021, NH–O: 1.796). In this way, the initial PT forming $-H^b$ occurs accompanied by the dihedral rotation of the 2-carboxamide group and the reformation of intramolecular HB for its stabilization.³⁵

2.2.2. Change in HOMO–LUMO Energies upon PCET between T-705 and $O_2^{\bullet-}$. Figure 5 shows the highest occupied molecular orbital (HOMO)–lowest unoccupied molecular orbital (LUMO) energy change along the PCET between T-705 and $O_2^{\bullet-}$, calculated by the DFT method. After the initial PT, some reactant species (conformers), that is, T-705^a, T-

705^b, the T-705⁻ ($-H^{a1}$, $-H^{a2}$, and $-H^b$), $O_2^{\bullet-}$, and HO_2^{\bullet} , coexist in the solution. The SOMO energy (Hartree) for HO_2^{\bullet} (−0.3142) is much lower than HOMO energies for T-705 and T-705⁻. Thus, the electron acceptor will be HO_2^{\bullet} , not $O_2^{\bullet-}$. Considering the CV results in Figure 1 that the generated HO_2^{\bullet} is not detected at the electrode reaction with the energy scanning shown in Figure 4, the electron donor will be $-H^b$ formed after the initial PT with dihedral rotation, for which the bold red line indicates the downhill energy relationship in Figure 5. Thus, this change in HOMO–LUMO energies upon PT between T-705 and $O_2^{\bullet-}$ forming $-H^b$ and HO_2^{\bullet} , with

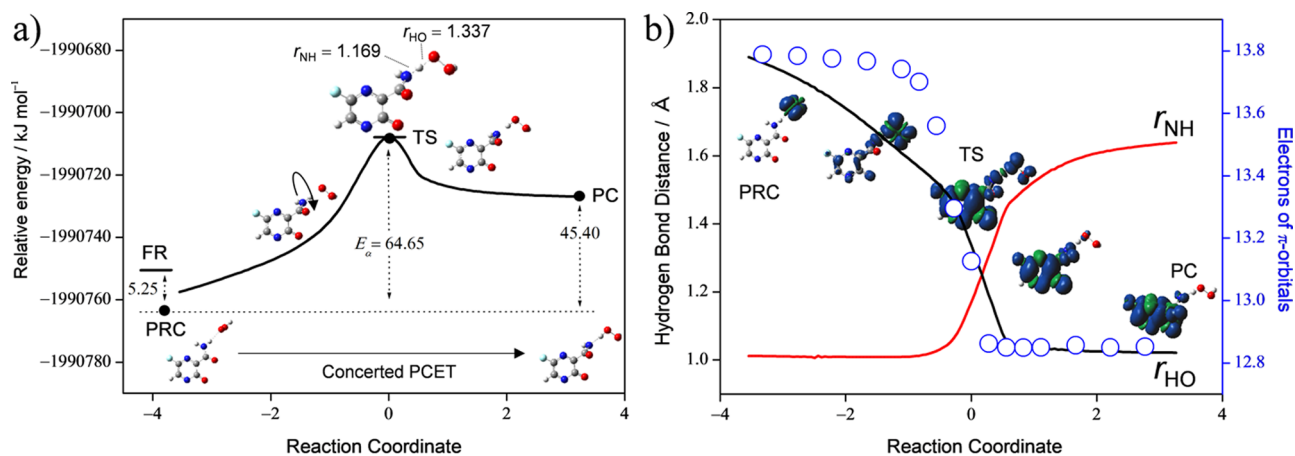


Figure 7. (a) IRC of the concerted PCET between T-705⁻ and HO₂[•] and structures along with the IRC, PRC (T-705⁻—HO₂[•]), TS with HB lengths (Å, r_{NH} and r_{HO}), and PC. (b) Changes in N—H bond (r_{NH} , red line) and H—O (r_{HO} , black line) bond lengths (Å, corresponding to the labels of the left vertical axes), and the number of electrons (open circles) on the π -orbitals in the T-705 moiety (corresponding to the labels of the right vertical axes). The calculations were performed using the DFT-(U)B3LYP/PCM/6-311+G(3df,2p) method. The NBO analyses obtained π -electrons and spin density distributions localizing the atoms constituting the radical before and after the PCET and at the TS shown in (b).

Table 1. ΔG° Values (kJ mol⁻¹, 298.15 K) of Six Diabatic Electronic States for PCET between O₂^{•-} and the Three Compounds (T-1105, T-705, and Catechol) in DMF, Calculated Using DFT at the B3LYP/PCM/6-311+G(3df,2p) Level

compounds	ΔG° /kJ mol ⁻¹									^d E _a /kJ mol ⁻¹
	^a PT1	PT2	PT3	PT4	ET1	ET2	ET3	^b concerted	^c total	
T-1105	8.2	-337.1	407.5	-20.6	475.2	129.8	-298.3	109.2	117.4	68.82
T-705	3.1	-348.8	398.8	-14.0	474.5	122.6	-290.2	108.5	111.7	64.65
catechol	-296.1	-336.7	365.1	-97.7	40.1	-0.4	-463.3	-98.2	-394.3	52.50

^aEach reaction process, PT1-PT4 and ET1-ET3. ^bConcerted values involve the sum of ΔG° s for ET2-PT4 (PT3-ET3). ^cTotal values involve the sum of ΔG° s for two PTs and one ET. ^dE_a values of concerted PCET for T-1105 and T-705 and concerted two-proton-coupled electron transfer for catechol.

that in the subsequent ET, is reasonable for the fact that HO₂[•] was eliminated in the CV.

The HOMO-LUMO relationship between the products after ET (i.e., -H^b-e and HO₂⁻) is reversed, which is rational for orbital energies in reverse ET (red dotted line in Figure 5). However, the HOMO (-0.2754) of the PT-forming H₂O₂ is lower than the HOMO (-0.1648) of HO₂⁻, making the reverse ET impossible. Thus, the second PT is dominant in determining the ET direction. Notably, only one conformer (-2H^b-e) is formed after the dihedral rotation of the 2-carboxamide group was adaptable for the radical cation due to the stability of intramolecular HB.

As a result, the HOMO-LUMO relationship analysis suggests that the plausible PCET mechanism involves two PTs and one ET with essential dihedral rotation for successful ET, eliminating HO₂[•] with good agreement with the electrochemical results.

2.2.3. Free Energy Analysis of PCET between T-705 and O₂^{•-}. In Figure 6, an equilibrium scheme and ΔG° values for the six diabatic electronic states in the PCET between T-705 and O₂^{•-} as calculated using DFT are shown. The important factors in determining the sequential processes shown in this scheme are the ΔG° s for the acid-base interaction and the redox potentials of the components. ET1 is strongly endergonic ($\Delta G^\circ = 474.5$ kJ mol⁻¹); thus, PT1 (3.1) coupled with the rotation of the dihedral angle around the 2-carboxamide group forming -H^b will first occur as suggested in the *in situ* electrolytic UV-vis spectral results shown in Figure 2. In the following pathways, both PT3 (398.9) and ET2 (122.6) are

endergonic, suggesting that the sequential PCET does not proceed contrary to the electrochemical results. This is because the optimized planar structures of intermediates at the electronic states (after PT3 and ET2) are thermodynamically stabilized due to intramolecular HB formation.³⁵ However, the ET2 is promoted by the following PT4 (-14.0), the second PT. As shown in the HOMO-LUMO relationship (Figure 5), the second PT is necessary for successful ET along the PCET. Thus, it is rational that the proton and electron are transferred in one kinetic process corresponding to the diagonal of the rectangle in Figure 5; labeled concerted PCET (108.5), rather than a sequential pathway of ET2-PT4.

2.2.4. Potential Energy Surfaces of the PCET between T-705 and O₂^{•-}. To clarify the oxidative degradation through the PCET mechanism, potential energy surfaces were investigated. After the initial PT forming T-705⁻ and HO₂[•] as free reactants (FRs), it is assumed that the reaction involves three elementary steps: (i) formation of the pre-reactive complex (PRC) from the FR, (ii) reaction to the product complex (PC) via a transition state (TS), and (iii) dissociation of the PC yielding free products. Furthermore, the structural and electronic changes during the reaction were analyzed with the natural bond orbital (NBO) calculations at the DFT-(U)B3LYP/PCM/6-311+G(3df,2p) level of theory in DMF. We started with an analysis of potential energy scanning for the stable PRC (T-705⁻—HO₂[•]) and PC (-2H^b-e—H₂O₂); then, optimized structures of plausible PRC and PC with the TS were obtained. In Figure 7, (a) energy profiles (ΔG° , kJ mol⁻¹) and (b) changes in N—H and H—O bond distances with the

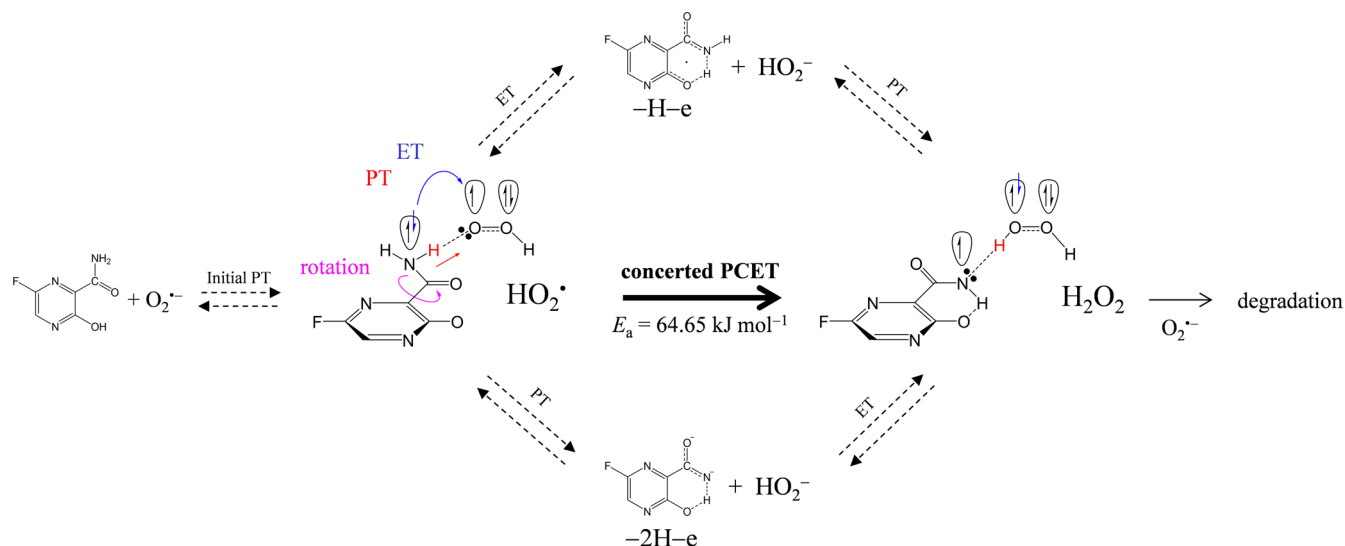


Figure 8. Mechanism of the oxidative degradation of T-705 by $\text{O}_2^{\bullet-}$ through the initial PT followed by concerted PCET with rotation of the dihedral angle around the 2-carboxamide group.

number of electrons on the π -orbital of T-705, along intrinsic reaction coordinate (IRC) for the PCET involving one ET and one PT forming the PC, are shown. The IRC shows that a concerted PCET occurs between T-705 $^-$ and HO_2^{\bullet} in one kinetic process via the TS of low activation energy (E_a) at $64.65 \text{ kJ mol}^{-1}$ without generating any intermediates.

Then, spin density distributions localizing the atoms consisting of the radical before and after the TS along the PCET are demonstrated in Figure 7b, showing that the radical localized on HO_2^{\bullet} in the initial system was transferred to T-705 $^-$ in the resulting reaction system. Changes in the spins on the electron donor side (T-705 $^-$) and acceptor side (HO_2^{\bullet}) are in good correlation with the changes in the π -electron of the T-705 $^-$ side. These results show that the π -electron of T-705 is transferred concertedly with the second PT.

For a comparative study, the ΔG° and the E_a of T-1105 and catechol along the PCET were also calculated (Table 1). The ΔG° s for the concerted PCET between HO_2^{\bullet} and the deprotonated anion, formed after the PT1, were obtained from the sum of the values for ET2 and PT4 (or for ET3 and PT3), respectively. Then, the total values of ΔG° s for the net PCET were obtained from the values for the two PTs and one ET. From a thermodynamic viewpoint, the total values cannot embody the energetic driving force of the net PCET for the T-1105 (117.4) and T-705 (111.7) because the ΔG° s for the unfeasible ET process have been summed in those. Conversely, the total value for the catechol (-394.3) embodies the energetic driving force, as shown in the CV (Figure 1d). Thus, the important factor for the net PCET pathway comprised PT1–ET2–PT4 to proceed as a sequential reaction is the ΔG° s for the individual reactions, rather than the total ΔG° s. Notably, both the total ΔG° and the ΔG° s of individual reactions along the plausible pathway, the sequential PCET comprised PT1–ET2–PT4 or the PT1–concerted PCET, indicate that the net PCET between T-705 (T-1105) and $\text{O}_2^{\bullet-}$ is unfeasible. Therefore, thermodynamic analyses did not clarify whether the PCET between T-705 (T-1105) and $\text{O}_2^{\bullet-}$ proceeds via a concerted or sequential pathway. However, the fact that the ΔG° result was opposite to the electrochemical result (Figure 1) implies that the kinetic insights into the degradation of T-705 (T-1105) through the PCET are needed.

The obtained E_a values are feasible for the concerted PCET, with a good correlation with the CV results. The notable finding was that the E_a value for T-705 (64.65) is close to that for catechol (52.50), whose kinetics are superior due to the concerted two-proton-coupled electron transfer pathway.²⁸ Careful observations of the changes in structures along the IRC (Figure 7b) indicate that the concerted PCET occurs simultaneously with the dihedral rotation of the 2-carboxamide group, implying that the rotation enables superior kinetics of the concerted PCET.

To clarify the oxidative degradation mechanism of the pyrazine antiviral drugs by $\text{O}_2^{\bullet-}$ through the thermodynamically unfeasible PCET, it is assumed that (i) the PCET proceeds through the concerted manner with superior kinetics apart from the thermodynamic energetics of the chemical species and (ii) the radical product of the PCET ($-\text{2H}^b-e$) irreversibly and quickly decomposes. Regarding (ii), the degradation of $-\text{2H}^b-e$, the electrochemical and calculation analyses do not clarify its mechanism; however, since the radical product unambiguously is undetectable using the *in situ* electrolytic UV–vis and ESR system, $-\text{2H}^b-e$ would quickly be decomposed. Thus, since the irreversible degradation of $-\text{2H}^b-e$ occurs following the PCET, the equilibrium of the PCET shown in Figure 6 will be promoted by the subsequent degradation.

In Figure 8, the net mechanism of the oxidative degradation of T-705 by $\text{O}_2^{\bullet-}$ through the initial PT and subsequent concerted PCET along the rotation of the dihedral angle around the 2-carboxamide group is shown. It is presumed that the high reactivity of T-705 and T-1105 with $\text{O}_2^{\bullet-}$, similar to that for catechol, is due to the mechanism. The PCET involving two PTs and one ET between catechol and $\text{O}_2^{\bullet-}$ based on quinone–hydroquinone π -conjugation forms the quinone radical anion as a product.²⁸ However, the quinone radical anion is moderately stable in aprotic solution, at least on the CV timescale and *in situ* ESR timescale; thus, the subsequent degradation is less associated with kinetics of the net PCET, that is, the degradation of $-\text{2H}^b-e$ promotes the net PCET between T-705 and $\text{O}_2^{\bullet-}$, demonstrating the catechol-like reactivity in the CV.

3. CONCLUSIONS

In **Conclusion**, we have investigated the reaction between electrogenerated $O_2^{\bullet-}$ and pyrazine antiviral drugs in DMF. As a result, we have concluded that

- Pyrazine antiviral drugs are easily decomposed by $O_2^{\bullet-}$ through the PCET involving two PTs and one ET.
- The concerted PCET after the initial PT occurs in one kinetic process via a TS without forming a high-energy intermediate.
- The net reaction involves rotation of the dihedral angle around the 2-carboxamide group along the PCET.

The dihedral rotation of the 2-carboxamide group is necessary for successful PCET; then, the concerted PCET is the key process for the oxidative degradation of the pyrazine antiviral drugs by $O_2^{\bullet-}$. Therefore, if we can design a new pyrazine drug that inhibits the rotation of the dihedral angle around the 2-carboxamide group along the PCET, it may be possible to develop hypodegradable antiviral drugs resistant to $O_2^{\bullet-}$.

Although the results presented in this manuscript are for a chemical reaction in an aprotic DMF solvent rather than a biological system, the PCET theory is adaptable to biological processes involving both protic and aprotic conditions in such a lipid bilayer. Therefore, we hope that the findings obtained in this study will show a mechanism for the biological degradation of pyrazine antiviral drugs by $O_2^{\bullet-}$ in the living body.

4. MATERIALS AND METHODS

4.1. Chemicals. T-1105, phenol, and catechol were purchased at the best available grade (>99.8%) from Tokyo Chemical Industry Co., Ltd. (Tokyo, Japan) and used as received. T-705 was purchased at the best available grade (>98.0%) from FUJIFILM Wako Pure Chemical Co., Ltd. (Osaka, Japan) and used as received. HPLC-grade anhydrous DMF and CH_3ONa (95% powder) used in electrochemical and spectrum measurements were purchased from Sigma-Aldrich Inc (Tokyo, Japan) and were used as received. TPAP (>98.0%, Tokyo Chemical Industry Co., Ltd.) was purchased and recrystallized many times from ethyl methanol, then dried overnight at 313.15 K (40.0 °C) under reduced pressure, and dried again for 2 h or more immediately before use. Further details are given in a previous paper.^{36,37} Ferrocene (Fc), used as a potential reference compound, was obtained from Nacalai Tesque Inc. (Kyoto, Japan) and purified by repeated sublimation under reduced pressure immediately before use.

4.2. Electrochemical and Electrolytic UV–Vis Spectral Measurements. Cyclic voltammetry was performed via a standard three-electrode system comprising a 1.0 mm-diameter GC working electrode, a coiled platinum counter electrode, and an Ag/AgNO₃ reference electrode (containing acetonitrile solution of 0.1 mol dm⁻³ tetrabutylammonium perchlorate and 0.01 mol dm⁻³ AgNO₃; BAS RE-5) at 298.15 K (25.0 °C) using an ECstat-301 electrochemical analyzer coupled to electrochemical software (EC-Frontier Co., Ltd.). The working electrode was polished with alumina paste on a polishing wheel before all experiments. The electrode was then rinsed with deionized water and acetone. After air drying, the electrode was ready to use. The reference electrode was calibrated with reference to the Fc⁺/Fc couple, and all potentials reported here are referenced to the potential of this couple (**Supporting Information**, CV parameter).^{28,30,35}

In situ electrolytic UV–vis spectra were recorded using an OCEAN HDX spectrometer (OptoSirius Co., Ltd.). The controlled-potential electrolysis was performed at room temperature in an OTTLE cell (path length: 1.0 mm) using a Pt mesh working electrode (**Supporting Information**, Figure S2). A coiled platinum counter electrode and an Ag/AgNO₃ reference electrode were also used in the UV–vis spectral measurements, as with the cyclic voltammetry measurements.²⁹

To prevent contamination by moisture, samples were prepared in a glovebox completely filled with N₂ gas. For the electrogeneration of $O_2^{\bullet-}$, a DMF solution containing 0.1 mol dm⁻³ tetrapropylammonium perchlorate (TPAP) as a supporting electrolyte was saturated with O₂ by air-bubbling the gas for ca. 2–3 min, and the gas was passed over the solutions during the electrochemical and electrolytic spectrometric measurements to maintain the concentration of O₂ at a constant level. The equilibrium concentration of O₂ was calculated as 4.8×10^{-3} mol dm⁻³.

4.3. Theoretical Calculations. All calculations were performed at the DFT level with the B3LYP hybrid functional, as implemented in the Gaussian 16 Program.³⁸ The geometry optimization, subsequent vibrational frequency calculations, and population analysis of each compound were performed by employing the standard split-valence triple ζ basis sets augmented by polarization 3df,2p and diffusion orbitals 6-311 + G(3df,2p). These functionals and basis sets were chosen because they have been shown to give good geometries in hydrogen transfer reactions involving PCET between phenolic compounds and $O_2^{\bullet-}$.³⁹ The solvent contributions of DMF, dimethylsulfoxide, acetonitrile, and water (**Supporting Information**, Tables S2–S5) to the standard Gibbs free energies were computed employing the PCM method at the default settings of Gaussian 16, which is widely employed in the description of the thermodynamic characteristics of solvation. The zero-point energies and thermal correction, with entropy, were used to convert the internal energies to standard Gibbs energy at 298.15 K. The NBO technique was used for electron and spin calculations of the population analyses.⁴⁰

■ ASSOCIATED CONTENT

Supporting Information

The Supporting Information is available free of charge at <https://pubs.acs.org/doi/10.1021/acsoomega.1c03230>.

CVs of $O_2/O_2^{\bullet-}$ in the presence of the acidic substrate; CV parameters; *in situ* electrolytic UV–vis (OTTLE) and ESR spectral system; conformers of T-1105 with ΔG s; comparison of ΔG s for the PCET in dimethyl sulfoxide, acetonitrile, water, and vacuum; charge distribution and natural population on the TS structures; and calculated geometries of TS (**PDF**)

■ AUTHOR INFORMATION

Corresponding Author

Tatsushi Nakayama – Gifu Pharmaceutical University, Gifu 501-1196, Japan; orcid.org/0000-0002-0346-2089; Phone: +81-58-230-8100; Email: tnakayama@gifu-pu.ac.jp; Fax: +81-58-230-8200

Author

Ryo Honda – United Graduate School of Drug Discovery and Medical Information Sciences, Gifu University, Gifu 501-1193, Japan

Complete contact information is available at:

<https://pubs.acs.org/10.1021/acsomega.1c03230>

Author Contributions

All authors contributed equally.

Funding

This research did not receive any specific grant from funding agencies in the public, commercial, or not-for-profit sectors.

Notes

The authors declare no competing financial interest.

ACKNOWLEDGMENTS

The authors would like to thank Sugawara for his experimental assistance.

NOMENCLATURE

PCET, proton-coupled electron transfer; RdRp, RNA-dependent RNA polymerase; ROS, reactive oxygen species; SFO, superoxide-facilitated oxidation; PT, proton transfer; ET, electron transfer; CV, cyclic voltammogram; GC, glassy carbon; OTTLE, optically transparent thin-layer electrochemical; ESR, electron spin resonance; DFT, density functional theory; B3LYP, Becke three-parameter Lee–Yang–Parr; PCM, polarized continuum model; HB, hydrogen bond; FR, free reactant; PRC, pre-reactive complex; PC, product complex; TS, transition state; NBO, natural bond orbital

REFERENCES

- (1) Wang, X.; Xia, S.; Wang, Q.; Xu, W.; Li, W.; Lu, L.; Jiang, S. Broad-Spectrum Coronavirus Fusion Inhibitors to Combat COVID-19 and Other Emerging Coronavirus Diseases. *Int. J. Mol. Sci.* **2020**, *21*, 3843.
- (2) Singh, A. K.; Singh, A.; Singh, R.; Misra, A. Remdesivir in COVID-19: A Critical Review of Pharmacology, Pre-Clinical and Clinical Studies. *Diabetes Metab Syndr.* **2020**, *14*, 641–648.
- (3) Malin, J. J.; Suárez, I.; Priesner, V.; Fätkenheuer, G.; Rybniker, J. Remdesivir against COVID-19 and Other Viral Diseases. *Clin. Microbiol. Rev.* **2021**, *34*, 1–21.
- (4) Khalili, J. S.; Zhu, H.; Mak, N. S. A.; Yan, Y.; Zhu, Y. Novel coronavirus treatment with ribavirin: Groundwork for an evaluation concerning COVID-19. *J. Med. Virol.* **2020**, *92*, 740–746.
- (5) Hutson, C. L.; Kondas, A. V.; Mauldin, M. R.; Doty, J. B.; Grossi, I. M.; Morgan, C. N.; Ostergaard, S. D.; Hughes, C. M.; Nakazawa, Y.; Kling, C.; Martin, B. E.; Ellison, J. A.; Carroll, D. D.; Gallardo-Romero, N. F.; Olson, V. A. Pharmacokinetics and Efficacy of a Potential Smallpox Therapeutic, Brincidofovir, in a Lethal Monkeypox Virus Animal Model. *mSphere* **2021**, *6*, No. e00927.
- (6) Li, D.-D.; Han, R.-M.; Liang, R.; Chen, C.-H.; Lai, W.; Zhang, J.-P.; Skibsted, L. H. Hydroxyl Radical Reaction with Trans-Resveratrol: Initial Carbon Radical Adduct Formation Followed by Rearrangement to Phenoxyl Radical. *J. Phys. Chem. B* **2012**, *116*, 7154–7161.
- (7) Furuta, Y.; Komeno, T.; Nakamura, T. Favipiravir (T-705), a Broad Spectrum Inhibitor of Viral RNA Polymerase. *Proc. Jpn. Acad. Ser. B Phys. Biol. Sci.* **2017**, *93*, 449–463.
- (8) Furuta, Y.; Gowen, B. B.; Takahashi, K.; Shiraki, K.; Smee, D. F.; Barnard, D. L. Favipiravir (T-705), a Novel Viral RNA Polymerase Inhibitor. *Antivir. Res.* **2013**, *100*, 446–454.
- (9) Tomita, Y.; Takeda, M.; Matsuyama, S. The Anti-Influenza Virus Drug Favipiravir Has Little Effect on Replication of SARS-CoV-2 in Cultured Cells. *Antimicrob. Agents Chemother.* **2021**, *65*, No. e00020.
- (10) Cai, L.; Sun, Y.; Song, Y.; Xu, L.; Bei, Z.; Zhang, D.; Dou, Y.; Wang, H. Viral Polymerase Inhibitors T-705 and T-1105 Are Potential Inhibitors of Zika Virus Replication. *Arch. Virol.* **2017**, *162*, 2847–2853.
- (11) Huchting, J.; Vanderlinden, E.; Winkler, M.; Nasser, H.; Naesens, L.; Meier, C. Prodrugs of the Phosphoribosylated Forms of Hydroxypyrazinecarboxamide Pseudobase T-705 and Its De-Fluoro Analogue T-1105 as Potent Influenza Virus Inhibitors. *J. Med. Chem.* **2018**, *61*, 6193–6210.
- (12) Gowen, B. B.; Wong, M.-H.; Jung, K.-H.; Smee, D. F.; Morrey, J. D.; Furuta, Y. Efficacy of Favipiravir (T-705) and T-1106 Pyrazine Derivatives in Phlebovirus Disease Models. *Antiviral Res.* **2010**, *86*, 121–127.
- (13) Hillen, H. S.; Kovic, G.; Farnung, L.; Dienemann, C.; Tegunov, D.; Cramer, P. Structure of Replicating SARS-CoV-2 Polymerase. *Nature* **2020**, *584*, 154–156.
- (14) Yin, W.; Mao, C.; Luan, X.; Shen, D.-D.; Shen, Q.; Su, H.; Wang, X.; Zhou, F.; Zhao, W.; Gao, M.; Chang, S.; Xie, Y.-C.; Tian, G.; Jiang, H.-W.; Tao, S.-C.; Shen, J.; Jiang, Y.; Jiang, H.; Xu, Y.; Zhang, S.; Zhang, Y.; Xu, H. E. Structural Basis for Inhibition of the RNA-Dependent RNA Polymerase from SARS-CoV-2 by Remdesivir. *Science* **2020**, *368*, 1499–1504.
- (15) Kaptein, S. J. F.; Jacobs, S.; Langendries, L.; Seldeslachts, L.; ter Horst, S.; Liesenborghs, L.; Hens, B.; Vergote, V.; Heylen, E.; Barthelemy, K.; Maas, E.; de Keyser, C.; Bervoets, L.; Rymenant, J.; van Buyten, T.; Zhang, X.; Abdelnabi, R.; Pang, J.; Williams, R.; Thibaut, H. J.; Dallmeier, K.; Boudewijns, R.; Wouters, J.; Augustijns, P.; Verougstraete, N.; Cawthorne, C.; Breuer, J.; Solas, C.; Weynand, B.; Annaert, P.; Spriet, I.; Vande Velde, G.; Neyts, J.; Rocha-Pereira, J.; Delang, L. Favipiravir at high doses has potent antiviral activity in SARS-CoV-2-infected hamsters, whereas hydroxychloroquine lacks activity. *Proc. Natl. Acad. Sci. U.S.A.* **2020**, *117*, 26955–26965.
- (16) Jockusch, S.; Tao, C.; Li, X.; Anderson, T. K.; Chien, M.; Kumar, S.; Russo, J. J.; Kirchdoerfer, R. N.; Ju, J. A Library of Nucleotide Analogues Terminate RNA Synthesis Catalyzed by Polymerases of Coronaviruses Causing SARS and COVID-19. **2020**, bioRxiv.
- (17) Quintal, S.; Pires da Silva, M. J.; Martins, S. R. M.; Sales, R.; Felix, V.; Drew, M. G. B.; Meireles, M. M.; Mourato, A.; Nunes, C. D.; Saraiva, M. S.; Machuqueiro, M.; Calhorda, M. J. Molybdenum-(II) Complexes with p-Substituted BIAN Ligands: Synthesis, Characterization, Biological Activity and Computational Study. *Dalton Trans.* **2019**, *48*, 8449.
- (18) Casadevall, A.; Pirofski, L.-a. In Fatal COVID-19, the Immune Response Can Control the Virus but Kill the Patient. *Proc. Natl. Acad. Sci. U.S.A.* **2020**, *117*, 30009–30011.
- (19) Hirouchi, T.; Ota, S.; Mashima, D.; Boku, R.; Yoshida, Y.; Iwata, K.; Shinada, K.; Matsumoto, T.; Morikawa, M.; Sato, T.; Shinoda, M.; Kamachi, K.; Shinkai, M. A Case of COVID-19 Pneumonia Successfully Treated with Favipiravir (Avigan) in Which Serum SARS-CoV-2 RNA Detected by LAMP Method Was Clinically Useful. *J. Infect. Chemother.* **2021**, *27*, 379–383.
- (20) Weigert, A.; von Knethen, A.; Fuhrmann, D.; Dehne, N.; Brüne, B. Redox-Signals and Macrophage Biology. *Mol. Aspect. Med.* **2018**, *63*, 70–87.
- (21) Agita, A.; Alsagaff, M. T. Inflammation, Immunity, and Hypertension. *Acta Med. Indones.* **2017**, *49*, 158–165.
- (22) Muri, J.; Kopf, M. Redox Regulation of Immunometabolism. *Nat. Rev. Immunol.* **2021**, *21*, 363–381.
- (23) Zhou, D.; Porter, W. R.; Zhang, G. G. Z. Drug Stability and Degradation Studies. In *Developing Solid Oral Dosage Forms: Pharmaceutical Theory and Practice*, 2nd ed.; Elsevier Inc., 2017; pp 113–149.
- (24) Nanni, E. J.; Birge, R. R.; Hubbard, L. M.; Morrison, M. M.; Sawyer, D. T. Oxidation and Dismutation of Superoxide Ion Solutions to Molecular Oxygen. Singlet vs. Triplet State. *Inorg. Chem.* **1981**, *20*, 737–741.

- (25) Nanni, E. J.; Stallings, M. D.; Sawyer, D. T. Does superoxide ion oxidize catechol, α -tocopherol, and ascorbic acid by direct electron transfer? *J. Am. Chem. Soc.* **1980**, *102*, 4481–4485.
- (26) Song, C.; Zhang, J. Electrocatalytic Oxygen Reduction Reaction. In *PEM Fuel Cell Electrocatalysts and Catalyst Layers: Fundamentals and Applications*; Springer Nature, 2008; pp 89–134.
- (27) Singh, P. S.; Evans, D. H. Study of the Electrochemical Reduction of Dioxygen in Acetonitrile in the Presence of Weak Acids. *J. Phys. Chem. B* **2006**, *110*, 637–644.
- (28) Nakayama, T.; Uno, B. Concerted Two-Proton-Coupled Electron Transfer from Catechols to Superoxide via Hydrogen Bonds. *Electrochim. Acta* **2016**, *208*, 304–309.
- (29) Nakayama, T.; Uno, B. Quinone-Hydroquinone π -Conjugated Redox Reaction Involving Proton-coupled Electron Transfer Plays an Important Role in Scavenging Superoxide by Polyphenolic Antioxidants. *Chem. Lett.* **2010**, *39*, 162–164.
- (30) Nakayama, T.; Uno, B. Importance of Proton-Coupled Electron Transfer from Natural Phenolic Compounds in Superoxide Scavenging. *Chem. Pharm. Bull.* **2015**, *63*, 967–973.
- (31) Nakayama, T.; Uno, B. Structural Properties of 4-Substituted Phenols Capable of Proton-Coupled Electron Transfer to Superoxide. *Int. J. Adv. Res. Chem. Sci.* **2016**, *3*, 11–19.
- (32) Biela, M.; Rimarčík, J.; Senajová, E.; Kleinová, A.; Klein, E. Antioxidant Action of Deprotonated Flavonoids: Thermodynamics of Sequential Proton-Loss Electron-Transfer. *Phytochemistry* **2020**, *180*, 112528.
- (33) Fridovich, I. Superoxide Dismutase. In *Encyclopedia of Biological Chemistry*, 2nd ed.; Elsevier Inc., 2013; pp 352–354.
- (34) Nakayama, T.; Honda, R. Electrochemical and Mechanistic Study of Superoxide Elimination by Mesalazine through Proton-Coupled Electron Transfer. *Pharmaceuticals* **2021**, *14*, 120.
- (35) Nakayama, T.; Okumura, N.; Uno, B. Complementary Effect of Intra- and Intermolecular Hydrogen Bonds on Electron Transfer in β -Hydroxy-Anthraquinone Derivatives. *J. Phys. Chem. B* **2020**, *124*, 848–860.
- (36) Okumura, N.; Uno, B. Electronic Spectra of the Electro-generated 1,4-Benzoquinone π -Dianion and the Strongly Hydrogen-Bonded Charge-Transfer Complex with Methanol. *Bull. Chem. Soc. Jpn.* **1999**, *72*, 1213–1217.
- (37) Katsumi, J.; Nakayama, T.; Esaka, Y.; Uno, B. Mechanistic Study on the Electrochemical Reduction of 9,10-Anthraquinone in the Presence of Hydrogen-Bond and Proton Donating Additives. *Anal. Sci.* **2012**, *28*, 257.
- (38) Frisch, G. W.; Schlegel, H. B.; Scuseria, G. E.; Robb, M. A.; Cheeseman, J. R.; Scalmani, G.; Barone, V.; Petersson, G. A.; Nakatsuji, H.; Li, X.; Caricato, M.; Marenich, A. V.; Bloino, J.; Janesko, B. G.; Gomperts, R.; Mennucci, B.; Hratch, D. J. *Gaussian 16*, Revision. B.01; Gaussian, Inc.: Wallingford, CT, 2016.
- (39) Quintero-Saumeth, J.; Rincón, D. A.; Doerr, M.; Daza, M. C. Concerted Double Proton-Transfer Electron-Transfer between Catechol and Superoxide Radical Anion. *Phys. Chem. Chem. Phys.* **2017**, *19*, 26179–26190.
- (40) Glendening, E. D.; Landis, C. R.; Weinhold, F. Natural Bond Orbital Methods. *Wiley Interdiscip. Rev.: Comput. Mol. Sci.* **2012**, *2*, 1–42.